

Magnetic and crystal electric field studies in the rare-earth-based square lattice antiferromagnet NdKNaNbO₅

S. Guchhait,¹ A. Painganoor,^{1,2,3} S. S. Islam,¹ J. Sichelschmidt,⁴ M. D. Le,⁵ N. B. Christensen,^{2,*} and R. Nath^{1,†}

¹*School of Physics, Indian Institute of Science Education and Research Thiruvananthapuram-695551, India*

²*Department of Physics, Technical University of Denmark, 2800 Kongens Lyngby, Denmark*

³*Institute Laue-Langevin, 38042 Grenoble Cedex 9, France*

⁴*Max Planck Institute for Chemical Physics of Solids, Nöthnitzer Str 40, 01187 Dresden, Germany*

⁵*ISIS Neutron and Muon Source, Science and Technology Facilities Council,*

Rutherford Appleton Laboratory, Didcot OX11 0QX, United Kingdom

(Dated: September 2, 2024)

The interplay of magnetic correlations, crystal electric field interactions, and spin-orbit coupling in low-dimensional frustrated magnets fosters novel ground states with unusual excitations. Here, we report the magnetic properties and crystal electric field (CEF) scheme of a rare-earth-based square-lattice antiferromagnet NdKNaNbO₅ investigated via magnetization, specific heat, electron spin resonance (ESR), and inelastic neutron scattering (INS) experiments. The low-temperature Curie-Weiss temperature $\theta_{CW} \simeq -0.6$ K implies net antiferromagnetic interactions between the Nd³⁺ ions. Two broad maxima are observed in the low temperature specific heat data in magnetic fields, indicating multilevel Schottky anomalies due to the effect of CEF. No magnetic long-range-order is detected down to 0.4 K. The CEF excitations of Kramers' ion Nd³⁺ ($J = 9/2$) probed via INS experiments evince dispersionless excitations characterizing the transitions among the CEF energy levels. The fit of the INS spectra enabled the mapping of the CEF Hamiltonian and the energy eigenvalues of the Kramers' doublets. The simulation using the obtained CEF parameters reproduces the broad maxima in specific heat in zero-field as well as in different applied fields. The significant contribution from $J_z = \pm 1/2$ state to the wave function of the ground state doublet indicates the role of strong quantum fluctuations at low temperatures. The magnetic ground state is found to be a Kramers' doublet with effective spin $J_{\text{eff}} = 1/2$ at low temperatures.

I. INTRODUCTION

Frustrated magnetism has been at the forefront of condensed matter research for decades since frustration compels the spin systems to resist magnetic long-range order (LRO) and to exhibit a variety of disordered ground states [1]. In a two-dimensional (2D) square lattice, frustration arises due to competing nearest-neighbor (NN) (J_1) and next-nearest-neighbor (NNN) (J_2) interactions along the edges and diagonals of a square, respectively. Based on the frustration ratio, $\alpha = J_2/J_1$, a series of fascinating phases are predicted theoretically for the spin-1/2 $J_1 - J_2$ model. The two most exciting ones are quantum spin-liquid (QSL) and spin-nematic phases that are predicted at the critical regimes $\alpha \simeq \pm 0.5$, respectively [2, 3]. However, to date, no experimental verifications of the existence of these phases have emerged. Most of the FSL systems experimentally realized so far are based on 3d transition metal ions, but none of them fall within the quantum critical regimes [4–10]. Unfortunately, none of the compounds feature a perfect square lattice, as the underlying crystal symmetries are lower than tetragonal [11].

Recently, rare-earth (4f) based antiferromagnets (AFM) with strong spin-orbit coupling (SOC) and crystal electric field (CEF) interactions offer an alternate route

to realize exotic quantum phenomena [12]. In such systems, CEF is typically weak compared to SOC and splits the spin-orbit entangled ground state into different singlet and doublet states. A system with an odd number of 4f electrons (Kramers' ion) forms Kramers' doublets and often behaves as an effective spin-1/2 system at a temperature that is low compared to the energy gap between the ground and first excited state doublets. The CEF controls the single ion ground state properties and determines the size and anisotropy of the magnetic moment. Further, from the wave functions of the CEF ground state and excited states, one can extract information about the role of quantum fluctuations, quantum tunneling, and anisotropic spin interactions of the system [13–15]. For instance, if the CEF ground state has significant $|J, J_z\rangle$ components with a large $|J_z|$, quantum fluctuations are suppressed and classical states are stabilized [13]. Here, J is the total angular momentum and J_z is the z -component of the angular momentum operator. On the other hand, if the CEF ground state has significant $|J, J_z\rangle$ components with a small $|J_z|$, it would facilitate quantum tunnelling and leads the system to host exotic quantum phenomena, such as QSL [16, 17]. Thus, in order to understand the nature of the magnetic ground state, especially for rare-earth-based systems, it is essential to analyze the CEF scheme. From the material perspective, while many rare-earth based frustrated magnets are studied [12, 18–29], systems featuring frustrated square lattice (FSL) have not yet received much attention due to the unavailability of model compounds.

* nbch@fysik.dtu.dk

† rnath@iisertvm.ac.in

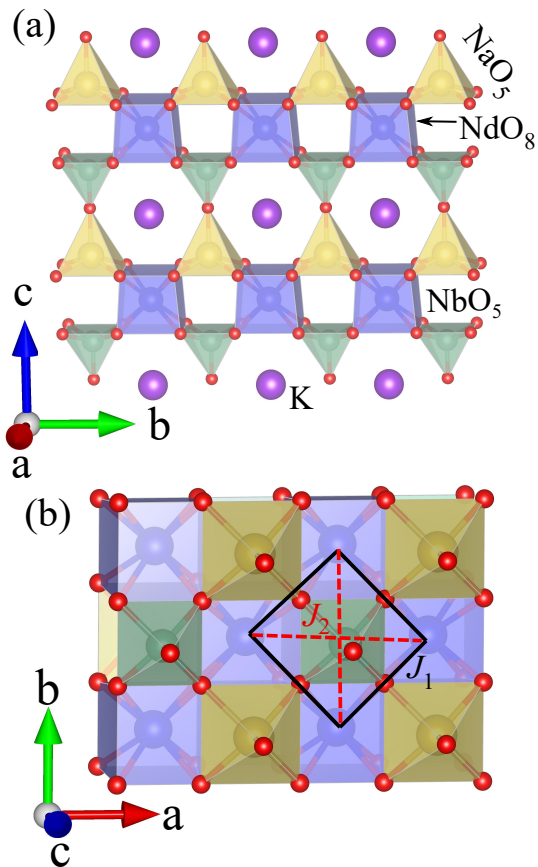


FIG. 1. (a) Crystal structure of NKNNO projected in the bc -plane that shows the stacking of two adjacent layers along the c -axis and their inter-layer connectivity via NbO_5 and NaO_5 square pyramids. (b) A section of the NdNaNbO_5 layer (square plane) in the ab -plane highlighting the interactions J_1 (along the sides of the square) and J_2 (along the diagonals of the square).

Recently, NaYbGeO_4 is reported to be a distorted square lattice compound, showing magnetic LRO at 0.21 K [30]. Similarly, another compound $\text{Bi}_2\text{YbO}_4\text{Cl}$ displays a perfect square lattice and doesn't order down to 0.09 K [31].

The family of compounds, LnKNaNbO_5 (Ln = Rare-earth) exist with a tetragonal structure (space group: $P4/nmm$ i.e. a perfect square lattice), without any structural disorder, making them favorable candidates to explore FSL model. NdKNaNbO_5 (NKNNO) belongs to the above family where distorted NdO_8 cubes are edge-shared with the basal edges of NbO_5 and NaO_5 square pyramids and form a layered structure in the ab -plane, as depicted in Fig. 1(b). Two adjacent NdNaNbO_5 -layers are interconnected via a common apical oxygen of NbO_5 and NaO_5 units along the c -axis [see Fig. 1(a)]. K^+ ions occupy the interstitial space. In each layer, Nd^{3+} ions form a perfect square lattice with NN exchange interaction (J_1) arising through Nd-O-Nd pathway while the NNN interaction (J_2) occurring via Nd-O-Nb-O-Nd or Nd-O-Na-O-Nd pathways [see Fig. 1(b)] [32]. Nd^{3+} is a Kramers ion with $4f^3$ configuration ($L = 6$, $S = 3/2$,

$J = 9/2$, and Landé g -factor $g = 0.73$) for which one expects five doublets with quantum numbers $J_z = \pm\frac{1}{2}, \pm\frac{3}{2}, \pm\frac{5}{2}, \pm\frac{7}{2},$ and $\pm\frac{9}{2}$. The low-temperature magnetic and CEF properties of this compound have not been studied yet. In this paper, we report a comprehensive study of the low-temperature magnetic properties and CEF excitations of Nd^{3+} in NKNNO by means of magnetization, specific heat, electron spin resonance (ESR), and inelastic neutron scattering (INS) measurements. No conventional magnetic LRO is detected down to 0.4 K. We could successfully model the INS spectra using the CEF Hamiltonian and extract information about the CEF energy levels. Finally, the specific heat calculated using the CEF parameters replicates the experimental specific heat data.

II. SYNTHESIS AND METHODS

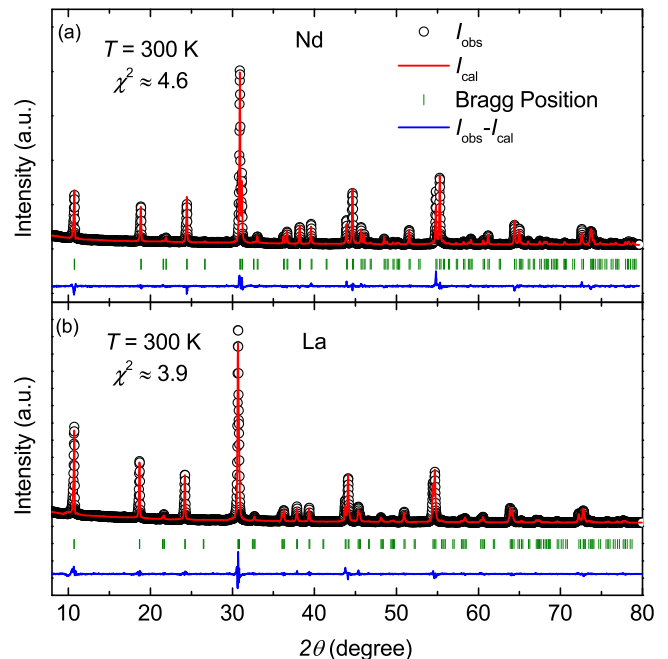


FIG. 2. Room temperature powder XRD patterns of (a) NKNNO and (b) LKNNO. Black circles denote the observed intensity and the red solid line represents the Rietveld fit. Green small vertical bars at the bottom show the Bragg peak positions and the blue solid line represents the difference between observed and calculated intensities. χ^2 represents the goodness-of-fit of the refinement.

Polycrystalline samples of NKNNO and the nonmagnetic isostructural compound LaKNaNbO_5 (LKNNO) were synthesized by the conventional solid-state reaction method. Stoichiometric amount of Ln_2O_3 ($\text{Ln} = \text{Nd}$ and La) (Aldrich, 99.9%), Na_2CO_3 (Aldrich, 99.9%), K_2CO_3 (Aldrich, 99.8%), and Nb_2O_5 (Aldrich, 99%) were ground thoroughly inside an Argon-filled glove box and pressed into pellets. Prior to grinding, preheating was done at 1000°C for one day for Ln_2O_3 and at 120°C for overnight

for Na_2CO_3 and K_2CO_3 . The pellets of LKNNO and NKNNNO were heated for several hours at 760°C and 800°C , respectively with intermediate grindings. In each intermediate grinding step, we added an extra amount (5 % excess) of Na_2CO_3 and K_2CO_3 to compensate the loss of Na and K during the heating process. The phase purity of the samples were checked by room temperature powder x-ray diffraction (XRD) measurement using a PANalytical powder diffractometer with Cu K_α radiation ($\lambda_{\text{avg}} \simeq 1.5418 \text{ \AA}$) (see Fig. 2). Rietveld refinement of the powder XRD patterns were performed using the FULLPROF software package [33], taking the initial structural parameters from Ref. [32]. The lattice parameters and unit cell volumes (V_{Cell}) obtained from the refinement are [$a = b = 5.8032(3) \text{ \AA}$, $c \simeq 8.2713(4) \text{ \AA}$, and $V_{\text{Cell}} \simeq 278.5 \text{ \AA}^3$] and [$a = b = 5.7367(2) \text{ \AA}$, $c = 8.2422(1) \text{ \AA}$, and $V_{\text{Cell}} \simeq 271.3 \text{ \AA}^3$] for LKNNO and NKNNNO compounds, respectively. These values are in close agreement with the previous report [32].

Magnetization (M) as a function of temperature (T) was measured in the temperature range 0.4–380 K in different magnetic fields using a superconducting quantum interference device (SQUID) (MPMS-3, Quantum Design) magnetometer. Isothermal magnetization (M vs H) was measured at $T = 0.4, 0.6, 1, 1.8, 3,$ and 5 K from 0 to 7 T. Measurements below 1.8 K were performed using a ^3He insert (iHelium3) to the SQUID magnetometer. Temperature-dependent specific heat at different fields (0-9 T) was measured on a sintered pellet in a large temperature range ($0.4 \text{ K} \leq T \leq 200 \text{ K}$) using the thermal relaxation technique in PPMS. A ^3He insert to the PPMS was used to measure specific heat below 2 K.

Electron spin resonance (ESR) experiments were performed on the powder sample using a standard continuous-wave spectrometer in the temperature range $3 \text{ K} \leq T \leq 30 \text{ K}$. We measured the power P absorbed by the sample from a transverse magnetic microwave field (X -band, $\nu = 9.4 \text{ GHz}$) as a function of an external static magnetic field. To improve the signal-to-noise ratio, a lock-in technique was employed. The final data were recorded as the derivative of the response signal $\frac{dP}{dH}$ as a function of the field. The ESR g -factor was calculated using the resonance condition, $g = \frac{h\nu}{\mu_B H_{\text{res}}}$, where h is Planck's constant, μ_B is the Bohr magneton, ν is the resonance frequency, and H_{res} is the corresponding resonance field.

For the zero-field inelastic neutron scattering (INS) experiment we used the direct geometry time-of-flight (TOF) spectrometer MARI at the ISIS Facility, Rutherford Appleton Laboratory, United Kingdom. Powder samples with total mass 3.5 g of NKNNNO and LKNNO were packed in an annular geometry inside Al cans which were cooled using a top-loading closed cycle refrigerator. Data were recorded at 6 and 200 K using incident neutron energies $E_i = 14, 40,$ and 100 meV and Gd chopper frequency 400 Hz. The three configurations gave elastic energy resolutions 0.3, 0.9, and 3 meV, respectively. The raw data were processed using the Mantid software [34].

III. RESULTS

A. Magnetization

Figure 3(a) presents the temperature dependent magnetic susceptibility $\chi[\equiv M/H]$ of NKNNNO measured at $\mu_0 H = 0.05$ and 1 T. No indication of magnetic LRO is observed down to 0.4 K. The inverse magnetic susceptibility, $1/\chi$, in the high-temperature region was well fitted by the modified Curie-Weiss (CW) law

$$\chi(T) = \chi_0 + \frac{C}{T - \theta_{\text{CW}}}. \quad (1)$$

Here, χ_0 is the combination of temperature-independent core diamagnetic (χ_{dia}) and Van-Vleck paramagnetic (χ_{VV}) susceptibilities. In the second term, C is the Curie constant and θ_{CW} is the CW temperature. The CW fit for $T \geq 100 \text{ K}$ yields $\chi_0 \simeq 5.14 \times 10^{-4} \text{ cm}^3/\text{mol}$, $C^{\text{HT}} \simeq 1.63 \text{ cm}^3\text{K}/\text{mol}$, and $\theta_{\text{CW}}^{\text{HT}} \simeq -66 \text{ K}$. From the C^{HT} value, the effective moment $\mu_{\text{eff}}^{\text{HT}} [= \sqrt{3k_B C^{\text{HT}}/N_A} \mu_B]$, where N_A is the Avogadro's number, μ_B is the Bohr magneton, and k_B is the Boltzmann constant] is calculated to be $\sim 3.61\mu_B$, which is close to the expected value $3.62\mu_B$ for a free Nd^{3+} ion. Here, the large negative value of $\theta_{\text{CW}}^{\text{HT}}$ does not indicate the presence of strong AFM interactions. It rather reflects the effect of CEF excitations at high temperatures. At high temperatures, all Kramers doublets get thermally populated and contribute to θ_{CW} .

At low temperatures, $1/\chi$ changes its slope due to depopulation of crystal field energy levels. A CW fit to $1/(\chi - \chi_{\text{VV}})$ in the low- T ($9 \text{ K} \leq T \leq 25 \text{ K}$) region results in $C^{\text{LT}} \simeq 0.55 \text{ cm}^3\text{K}/\text{mol}$ and $\theta_{\text{CW}}^{\text{LT}} \simeq -0.6 \text{ K}$. The value of χ_{VV} is obtained from the magnetization isotherm analysis (discussed later). The negative value of $\theta_{\text{CW}}^{\text{LT}}$ suggests a weak AFM net interaction among the Nd^{3+} ions. The obtained C^{LT} value corresponds to an effective moment of $\mu_{\text{eff}}^{\text{LT}} \simeq 2.1\mu_B$. The reduced value of effective moment [$\mu_{\text{eff}} = g\sqrt{J_{\text{eff}}(J_{\text{eff}} + 1)}\mu_B$] at low- T s corresponds to pseudo spin $J_{\text{eff}} = 1/2$ with $g \simeq 2.45$, suggesting that the lowest Kramers' doublet is the ground state. As we shall see below, this g -value matches with the one obtained from the ESR experiments at low- T s.

In order to estimate the energy splitting between the ground state and first excited Kramers' doublets in the CEF scheme, $1/\chi(T)$ was also fitted by the effective two-level CEF expression [35, 36]

$$\chi(T) = \chi_0 + \frac{1}{8(T - \theta_{\text{CW}})} \times \left[\frac{\mu_{\text{eff},0}^2 + \mu_{\text{eff},1}^2 e\left(-\frac{\Delta}{k_B T}\right)}{1 + e\left(-\frac{\Delta}{k_B T}\right)} \right]. \quad (2)$$

Here, Δ/k_B is the energy difference between the ground state and the first excited CEF levels. $\mu_{\text{eff},0}$ and $\mu_{\text{eff},1}$ are the effective moments of the ground state and first excited CEF levels, respectively. The two-level CEF fit for $T \leq 20 \text{ K}$ yields $\chi_0 \simeq 7 \times 10^{-3} \text{ cm}^3/\text{mol}$, $\mu_{\text{eff},0} \simeq 2.06\mu_B/\text{Nd}^{3+}$, $\mu_{\text{eff},1} \simeq 2.2\mu_B/\text{Nd}^{3+}$, $\Delta/k_B \simeq 18 \text{ K}$, and

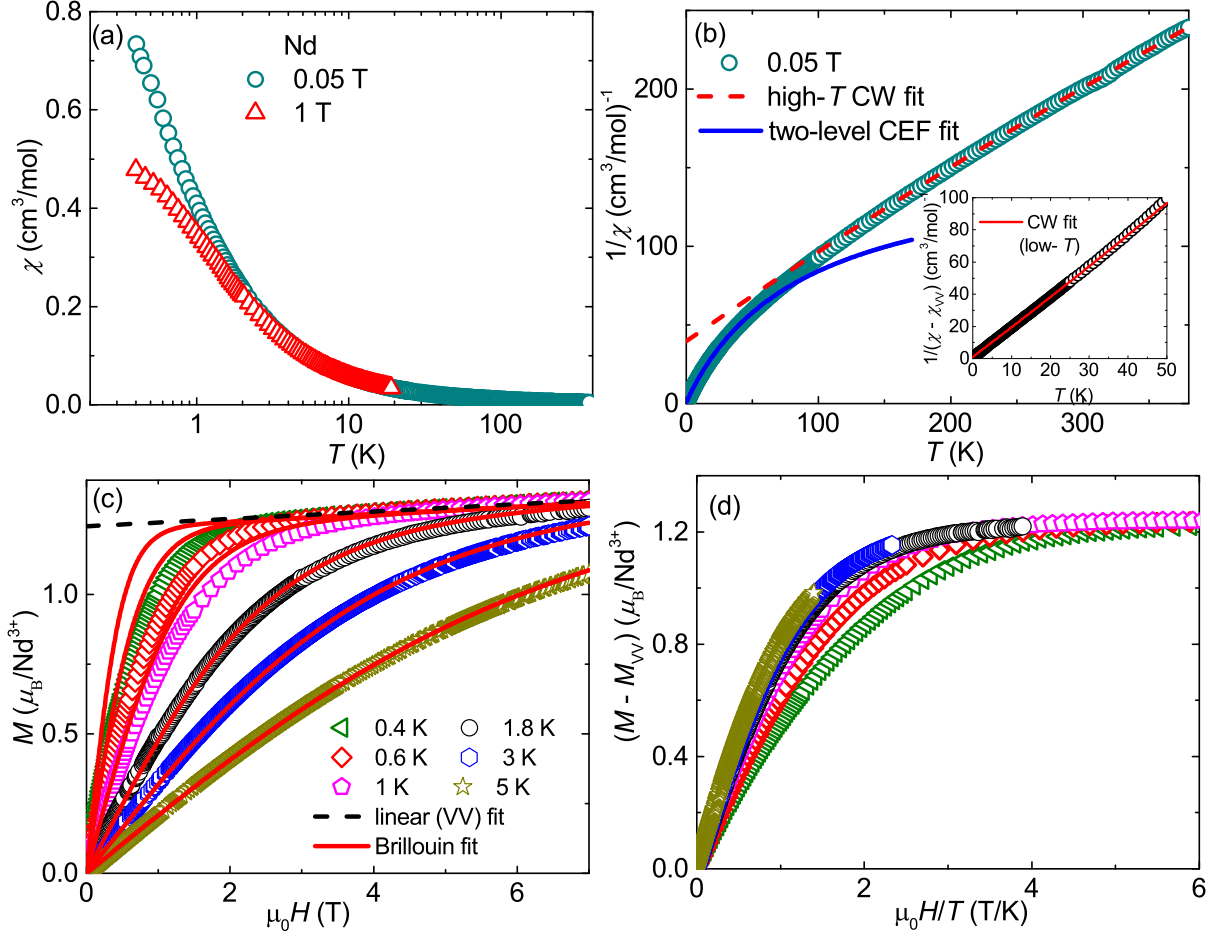


FIG. 3. (a) χ vs T of NKNNO measured at $\mu_0 H = 0.05$ and 1 T. (b) $1/\chi$ vs T at $\mu_0 H = 0.05$ T. The red dashed line is the high- T CW fit and the solid blue line indicates the two-level CEF fit. Inset: $1/(\chi - \chi_{VV})$ vs T and the solid line is CW fit in the low- T region. (c) M vs H at $T = 0.4, 0.6, 1, 1.8, 3,$ and 5 K. The dashed line represents a linear fit to the high-field data for $T = 0.4$ K. The solid lines represent the Brillouin function fits with $J_{\text{eff}} = 1/2$ Nd^{3+} moment. (d) $(M - M_{VV})$ vs $\mu_0 H/T$ to visualize the scaling of magnetization curves.

$\theta_{\text{CW}} \simeq -0.32$ K. It should be noted that this is a simple two-level model fit that neglects higher-lying Kramers doublets for a tentative estimation of the energy difference between ground and first excited states. Nevertheless, as we shall see the obtained χ_0 matches with χ_{VV} and Δ/k_B matches with the estimated gap between the ground state and first excited state doublets from INS data.

Isothermal magnetization curves (M vs $\mu_0 H$) measured at $T = 0.4, 0.6, 1, 1.8, 3,$ and 5 K are shown in Fig. 3(c). The magnetization at 0.4 K almost saturates in a low field of around 2 T, which is consistent with the low $\theta_{\text{CW}}^{\text{LT}}$ value. A slow increase of magnetization in higher fields can be attributed to the Van-Vleck susceptibility (χ_{VV}). From the linear fit of the curve in the high-field region ($\mu_0 H \geq 5.5$ T), we obtained a slope of around $\chi_{VV} \simeq 0.0125 \mu_B/T = 0.007 \text{ cm}^3/\text{mol}$, which was used in the low- T $\chi(T)$ analysis presented above. The fit is extrapolated down to zero-field and from the

y -axis intercept, we obtained the saturation magnetization $M_S \simeq 1.24 \mu_B$, which points towards $J_{\text{eff}} = 1/2$ ground state with $g \simeq 2.48$. This value of g is also in close agreement with the ESR results which will be presented below.

Magnetic isotherms at slightly higher temperatures ($T > 1$ K) can be modeled by the following expression [37]

$$M(H) = \chi_{VV} H + N_A g \mu_B J_{\text{eff}} B_{J_{\text{eff}}}(x). \quad (3)$$

Here, $B_{J_{\text{eff}}}(x)$ is the Brillouin function which can be written as $B_{J_{\text{eff}}}(x) = \frac{(2J_{\text{eff}}+1)}{2J_{\text{eff}}} \coth \left[\frac{(2J_{\text{eff}}+1)}{2J_{\text{eff}}} x \right] - \frac{1}{2J_{\text{eff}}} \coth \left(\frac{x}{2J_{\text{eff}}} \right)$ and $x = g \mu_B J_{\text{eff}} H / k_B T$ [38]. For this fit, we fixed $J_{\text{eff}} = 1/2$, $\chi_{VV} \simeq 0.007 \text{ cm}^3/\text{mol}$, and $g \simeq 2.47$ (obtained from ESR). For high temperatures ($T = 1.8, 3,$ and 5 K), Eq. (3) fits well to the isotherms while below 1 K, the fit deviates significantly from the experimental data, signaling the emergence of magnetic correlations. To illustrate this feature more clearly, we plot

ted the Van-Vleck corrected M (i.e. $M - M_{\text{VV}}$) vs $\mu_0 H$ scaled with respect to the temperature in Fig. 3(d). For $T \geq 1$ K, all the $M - M_{\text{VV}}$ vs $\mu_0 H/T$ curves collapse onto a single curve, reflecting the paramagnetic nature of the spins. However, for $T < 1$ K the curves show clear deviation from this pattern, demonstrating the development of magnetic correlations on a temperature scale comparable to the low $\theta_{\text{CW}}^{\text{LT}}$ value.

B. Specific Heat

The temperature-dependent specific heat, $C_p(T)$, of NKNNO measured down to 0.4 K and in different applied fields is shown in Fig. 4. In a magnetic insulator, the total specific heat $C_p(T)$ is the sum of the lattice contribution [$C_{\text{ph}}(T)$], which dominates in the high-temperature region and the magnetic part [$C_{\text{mag}}(T)$], which dominates in the low-temperature region. We estimated $C_{\text{ph}}(T)$ by measuring the zero-field specific heat of the non-magnetic isostructural compound LKNNO [see Fig. 4(a)] down to 2 K. The low-temperature specific heat data of LKNNO is fitted by βT^3 and further extrapolated down to 0.4 K. The estimated lattice specific heat of LKNNO was scaled with respect to NKNNO by taking the ratio of their atomic masses [39] and then subtracted from the total specific heat of NKNNO. The obtained $C_{\text{mag}}(T)$ at different fields is plotted in Fig. 4(b).

The zero-field C_{mag} shows a broad maximum at around $T^* \sim 9$ K and an upturn at $T < 1$ K. The low-temperature upturn can be attributed to the buildup of short range magnetic correlations, since the value of $\theta_{\text{CW}}^{\text{LT}}$ is of the same order of magnitude. With increasing field, the position of the high-temperature maximum remains almost unchanged and another broad maximum (T^{**}) appears at low-temperature. The latter peak shifts to high temperatures with increasing field. Both peaks are also found to broaden with increasing field. In high magnetic fields ($\mu_0 H > 6$ T), the T^* and T^{**} peaks merge and form a single broad high-temperature peak. Similar behaviour is reported for some Er^{3+} and Yb^{3+} -based compounds and ascribed to a multilevel Schottky effect due to the CEF levels and their splitting in applied fields [40–42]. As discussed later, the broad maximum at T^{**} corresponds to the transition between two Zeeman levels of the ground state doublet while the peak at T^* represents the transitions between the ground state and first excited state doublets as well as among the excited state doublets [see Fig. 9(b)].

The magnetic entropy [$\Delta S(T)$] released at different fields, estimated by integrating C_{mag}/T over the entire temperature range is presented in Fig. 4(c). In zero-field and 1 T, $\Delta S(T)$ couldn't be estimated reliably as our measurements down to 0.4 K could not reproduce the entire low-temperature anomaly. However, at $\mu_0 H = 2$ T where two broad maxima are distinctly visible, $\Delta S(T)$ features a plateau with $\Delta S \sim 5.7$ J mol $^{-1}$ K $^{-1}$ in the low-temperature regime before it attains a tendency of

saturation to $\Delta S \sim R \ln 4 \sim 11.5$ J mol $^{-1}$ K $^{-1}$ (R is the universal gas constant) at high temperatures. Indeed, the value of $\Delta S \sim 5.7$ J mol $^{-1}$ K $^{-1}$ matches with $R \ln 2$, expected for a $J_{\text{eff}} = 1/2$ system. This further endorses that the ground state is governed by the lowest Kramers' doublet with $J_{\text{eff}} = 1/2$ [36]. The $\Delta S \sim 12$ J mol $^{-1}$ K $^{-1}$ value at 50 K is still smaller than the expected value for Nd^{3+} ($\sim R \ln 10 = 19.14$ J mol $^{-1}$ K $^{-1}$) ion with $J = 9/2$.

In order to further confirm the $J_{\text{eff}} = 1/2$ ground state, the broad maximum at T^{**} in $C_{\text{mag}}(T)$ was fitted by the two-level Schottky function [38]

$$C_{\text{Sch}}(T, H) = fR \left(\frac{\Delta_{\text{I}}}{k_{\text{B}}T} \right)^2 \frac{e^{\left(\frac{\Delta_{\text{I}}}{k_{\text{B}}T}\right)}}{\left[e^{\left(\frac{\Delta_{\text{I}}}{k_{\text{B}}T}\right)} + 1 \right]^2}. \quad (4)$$

Here, f is the molar fraction of free spins contributing to the Schottky anomaly and $\Delta_{\text{I}}/k_{\text{B}}$ is the energy gap between two Zeeman levels of the ground state Kramers doublet. The fit of C_{mag} at 2 T in the temperature range 0.6-1.6 K yields $f \simeq 1$ and $\Delta_{\text{I}}/k_{\text{B}} \simeq 2.4$ K. We then extrapolated the fit from 0.4 to 30 K, as shown in Fig. 4(b). The calculated entropy corresponding to the maximum at T^{**} saturates to a value $\sim R \ln 2$ at around 6 K [see the inset of Fig. 4(c)], reflecting Kramers' doublet ground state with $J_{\text{eff}} = 1/2$. The value $\Delta_{\text{I}}/k_{\text{B}}$ obtained in different fields is shown in the inset of Fig. 4(b). As expected, $\Delta_{\text{I}}/k_{\text{B}}$ varies linearly with field and a straight line fit ($\Delta_{\text{I}} = \Delta_0 + g\mu_{\text{B}}H$) [43] yields $g \simeq 2.3$, consistent with the ESR results. A fit using Eq. (4) to the second broad maximum at T^* results in no change in the gap ($\Delta_{\text{II}} \sim 21$ K) value with field.

C. ESR

The results of ESR measurements on NKNNO are presented in Fig. 5. The inset of Fig. 5(a) illustrates a typical ESR spectrum at $T = 3$ K. We fitted the spectra at different temperatures using a powder-averaged Lorentzian line shape. The fit reproduces the spectral shape very well at $T = 3$ K, yielding an average low-temperature g -factor of $g \simeq 2.47$. As shown in Fig. 5(a), the g value decreases slowly with increasing temperature and attains a constant value of 2.32 above 30 K. Figure 5(b) presents the ESR linewidth as a function temperature. It depicts a broad maximum at ~ 10 K that matches with T^* observed in specific heat, mimicking the crystal field excitations.

Below the broad maximum, the relaxation (ΔH) can be fitted by [44]

$$\Delta H \propto \frac{1}{e^{\Delta^{\text{esr}}/k_{\text{B}}T} - 1}. \quad (5)$$

Here, Δ^{esr} represents the energy gap in the CEF scheme and μ_0 is the permeability in free space. This exponential behavior implies the spin-lattice relaxation process

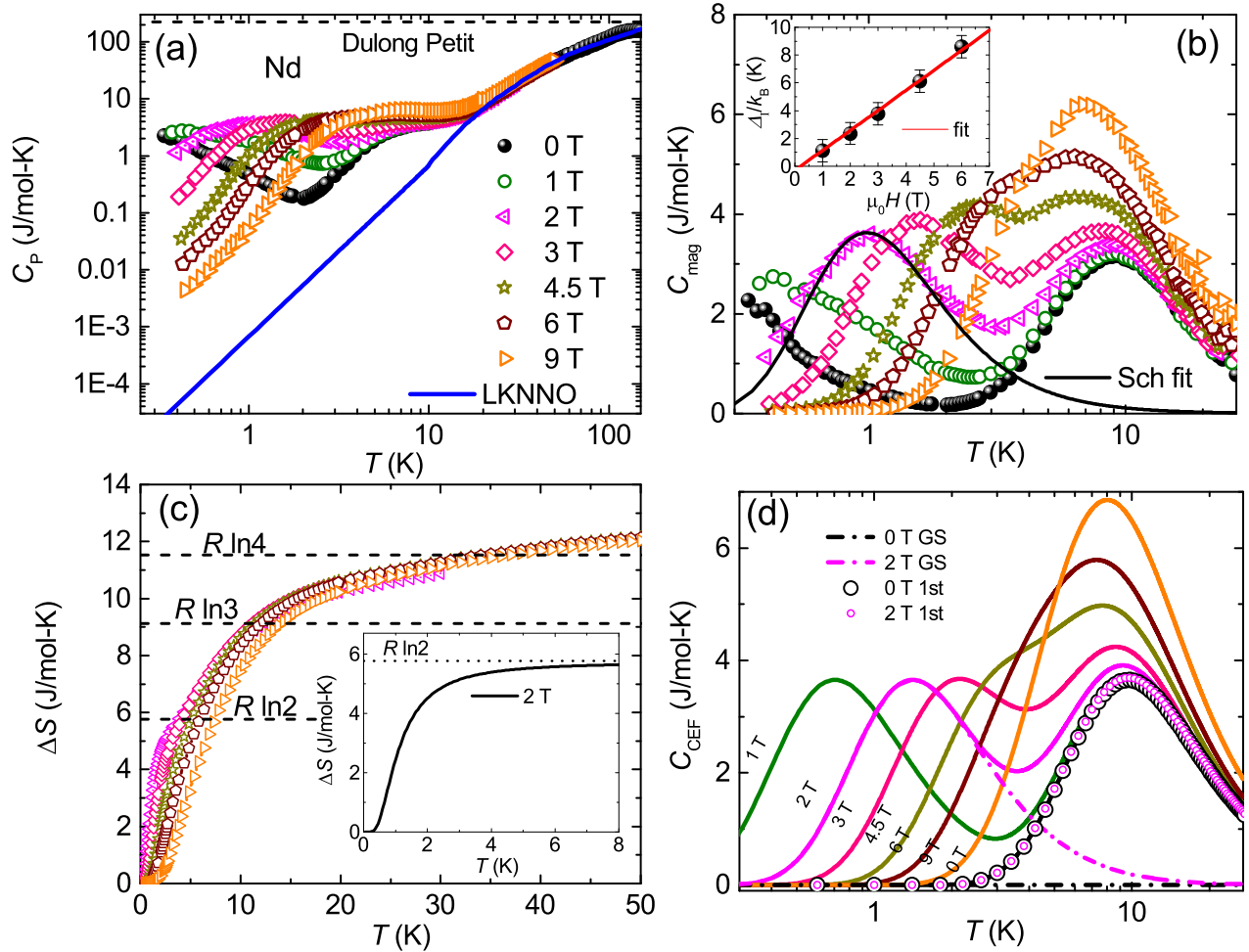


FIG. 4. (a) C_p vs T of NKNNO measured in different applied magnetic fields. The blue solid line represents the phonon contribution (C_{ph}) of the nonmagnetic compound LKNNO. The horizontal dashed line stands for the Dulong-Petit value $3nR$ (n is the number of atoms per formula unit). (b) C_{mag} vs T in different magnetic fields. The solid line is the Schottky fit using Eq. (4) to the 2 T data. Inset: ΔI vs H along with the linear fit. (c) Entropy change (ΔS) vs T in different magnetic fields. Inset: ΔS vs T associated with the broad maximum at T^{**} for the 2 T data. (d) Calculated C_{CEF} vs T in different magnetic fields, as discussed in the text. The solid lines represent C_{CEF} with contributions from the ground state and first excited state doublets in the CEF scheme. The dash-dotted lines and open circles separately show the contributions from ground state excitations and excitations between the ground state and first excited states, respectively in zero-field and $\mu_0 H = 2$ T.

is dominated by an Orbach process due to the CEF [45]. Through SOC, this process involves a phonon absorption to and emission from a CEF energy level. The fit in the low temperature regime (2.8-5 K) returns $\Delta^{est} \simeq 22.2$ K, which is consistent with the energy gap (2.1 meV) between the ground and first excited doublets observed in the INS data.

D. Inelastic Neutron Scattering

Figure 6 presents the color plots of the INS spectra of NKNNO and LKNNO measured using neutrons of incident energy $E_i = 40$ meV at temperatures $T = 6$ and 200 K and $E_i = 14$ meV at $T = 6$ K. For NKNNO, we observed a broad band of excitations around 20 meV, which

are more pronounced at low-temperature ($T = 6$ K) than at elevated temperatures and decrease in intensity with increasing Q , as we shall show below. Furthermore, no low- Q excitations are observed for the non-magnetic analogue compound LKNNO. These observations are consistent with a magnetic origin for the 20 meV excitation band in NKNNO. Given that the energy resolution for the chosen experimental setup is 0.9 meV which is smaller than the width of the excitation band, we interpret it as arising from a group of closely spaced crystal field excitations, each of which is dispersionless, because CEF excitations are single-ion properties. In order to extract these high-energy CEF excitations from the background due to phonon scattering, we subtracted the INS spectra of nonmagnetic LKNNO in which the excitations are purely phononic, from the spectra of NKNNO. Figure 7 depicts

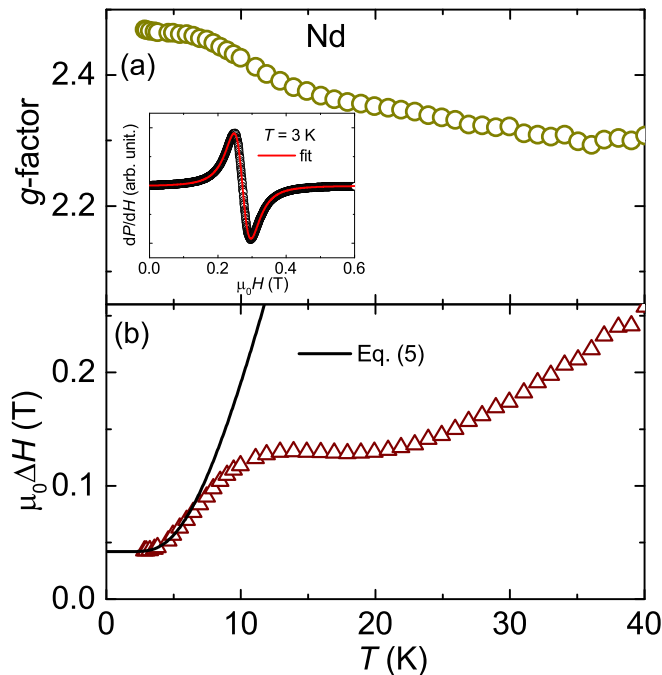


FIG. 5. (a) g -factor as a function of temperature for NKNNO. Inset: ESR spectra at $T = 3$ K. The solid line is a Lorentzian fit. (b) Temperature dependent ESR linewidth ($\mu_0\Delta H$). The solid line is the fit using Eq. (5).

the resulting phonon-subtracted INS spectra of NKNNO at $T = 6$ and 200 K. The intensity of the CEF excitations near 2 and 20 meV decrease with increasing Q ($= |\vec{Q}|$), as expected because of the magnetic form-factor [$F(Q)$] in the neutron scattering cross section. We calculated $F^2(Q)$ for Nd^{3+} ion using the dipole approximation (see Appendix A for details on the magnetic cross-section and the magnetic form-factor) and compared with the experimental INS intensity in Fig. 8(a). The calculated intensity decreases monotonously with increasing Q and reproduces the experimental data very well at $T = 6$ K. The intensity of the CEF excitations furthermore diminishes with rising temperature due to thermal broadening and because of depopulation of the ground state Kramers' doublet.

For a clear visualization of the CEF modes and to fit the INS data, we created a 2D plot of intensity versus energy transfer by integrating the phonon subtracted INS data in the wave-vector $0 \leq Q \leq 3 \text{ \AA}^{-1}$ regime, as shown in Fig. 7(c) and (d) for $T = 6$ K and 200 K, respectively. The observed strong signal at $\hbar\omega = 0$ meV corresponds to the quasielastic neutron scattering. In addition, we observed four CEF excitations for $T = 6$ K at around 2.3, 19.2, 20.9, and 22.6 meV with the 2.3 meV excited Kramers doublet appearing as a weak but distinct shoulder on the dominant quasielastic signal [see inset of Fig. 7(c)]. There exists a weak low-energy mode in the spectra obtained with $E_i = 14$ meV for which the energy resolution is 0.3 meV [see Fig. 6(c)]. The inset

of Fig. 7(c) shows the low-energy peak cleanly separated from the $\hbar\omega = 0$ peak. The momentum dependence of the low-energy excitations shown in Fig. 8(a) confirms its magnetic origin. In the low-temperature spectrum ($T = 6$ K), no peaks are observed near -20 meV in the negative energy transfer regions (reflecting transitions from excited state Kramers doublet to the ground state doublet) at low temperatures. On the other hand, in the high temperature ($T = 200$ K) spectrum, the increasing thermal population of excited CEF levels implies that such transitions become allowed and are observed as low-intensity peaks at negative energy transfers [46]. Figure 8(b) was produced using neutrons with higher incident energy $E_i = 100$ meV and shows that at $T = 6$ K there are no additional high-energy CEF transitions for energy transfers up to $\hbar\omega = 65$ meV. Therefore, we used only the INS spectra corresponding to $E_i = 40$ meV for the CEF analysis.

E. CEF Analysis

The INS intensity versus energy transfer data can be analyzed using the CEF Hamiltonian. According to the Stevens convention, the CEF Hamiltonian can be written as [47]

$$\mathcal{H}_{\text{CEF}} = \sum_{l,m} B_l^m \hat{O}_l^m. \quad (6)$$

Here, \hat{O}_l^m are the Stevens operators [47, 48], which are related to the angular momentum operators (see Appendix B). B_l^m are the multiplicative factors called CEF parameters, which are related to the electronic structure of the rare-earth materials (see Appendix B). Here, the even integer l varies from 0 to 6 for f electrons and the integer m ranges from $-l$ to l . In NKNNO, Nd^{3+} ion has a C_{4v} symmetric crystal field environment, which indicates that only five CEF parameters (B_2^0 , B_4^0 , B_6^0 , B_4^4 , and B_6^4) are nonzero [48]. Therefore, the CEF model Hamiltonian can be expressed as

$$\mathcal{H}_{\text{CEF}} = B_2^0 \hat{O}_2^0 + B_4^0 \hat{O}_4^0 + B_4^4 \hat{O}_4^4 + B_6^0 \hat{O}_6^0 + B_6^4 \hat{O}_6^4. \quad (7)$$

As presented in Fig. 7(c) and (d), we fitted the 6 K and 200 K data simultaneously using the above CEF model with the help of Mantid software [34, 49]. For this fit, we used the starting CEF parameters of the point-charge model where we assumed that the surrounding ligands are electrostatic point charges [48]. The obtained best-fit CEF parameters that determine the correct CEF Hamiltonian of this system are tabulated in Table I.

Next, we diagonalized the Hamiltonian and obtained the CEF energy eigenvalues of the compound. The obtained energy eigenvalues are 0, 2.11, 19.22, 20.92, and 22.7 meV, corresponding to five doublets, as depicted in Fig. 9. The peaks observed in the INS data at $T = 6$ K [Fig. 7(c)] correspond to the transitions I, II, III, and

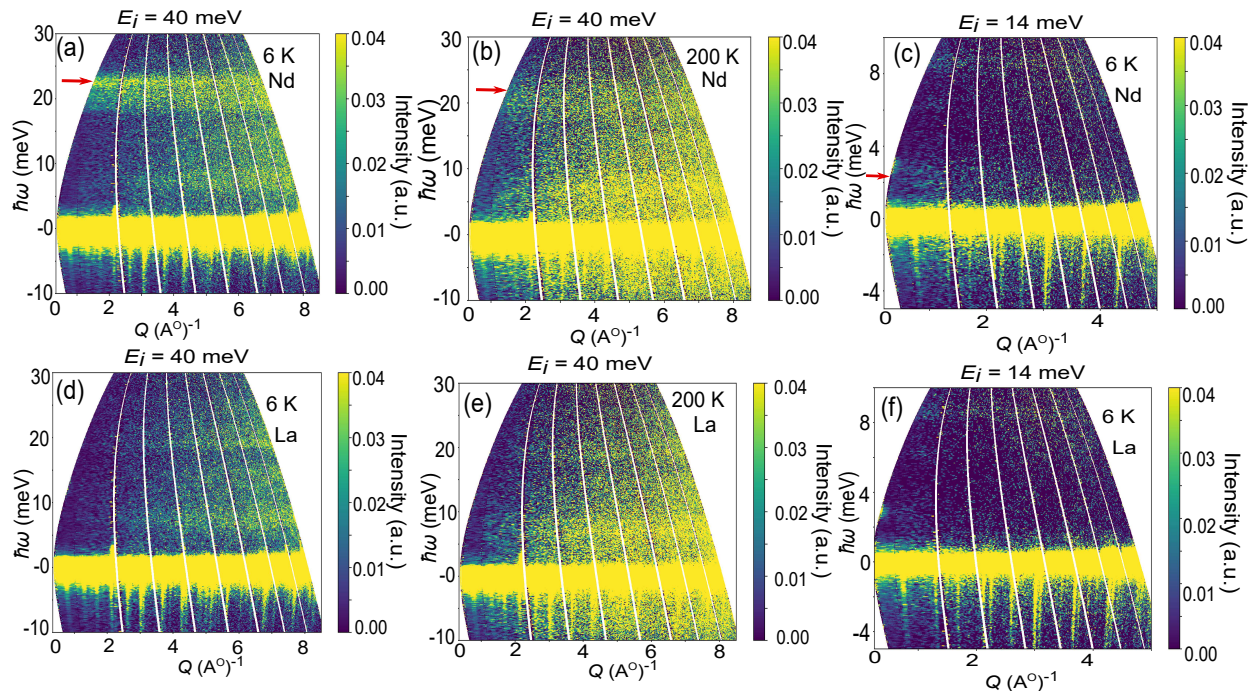


FIG. 6. Raw INS spectra $S(Q, \omega)$ of (a-b) NKNNO and (d-e) LKNNO (intensity as a function of energy and momentum transfers) at two different temperatures for $E_i = 40$ meV. The red arrows indicate the high-energy CEF excitations in the NKNNO spectra. Raw INS spectra of (c) NKNNO and (f) LKNNO at $T = 6$ K for $E_i = 14$ meV. The red arrow marks the CEF excitations at around 2.1 meV.

TABLE I. Fitted CEF parameters for NKNNO.

B_l^m (meV)	Values
B_2^0	8.087×10^{-2}
B_4^0	-1.772×10^{-3}
B_4^4	-5.451×10^{-3}
B_6^0	-3.835×10^{-5}
B_6^4	1.766×10^{-3}

IV, respectively between the ground state and excited states [50].

From the CEF Hamiltonian [Eq. (7)], the wave functions corresponding to all the Kramers' doublets can be expressed as

$$|\psi_k, \pm\rangle = \sum_{m_J = -\frac{9}{2}}^{m_J = \frac{9}{2}} C_{m_J}^{k, \pm} \left| J = \frac{9}{2}, m_J \right\rangle. \quad (8)$$

Here, $C_{m_J}^{k, \pm}$ are the weighted coefficients of the eigenstates. The full list of energy eigenvalues and the corresponding coefficients ($C_{m_J}^{k, \pm}$) of different eigenstates for NKNNO are listed in Table II. The wave function of the ground state doublet (lowest energy doublet) is obtained to be

$$|\psi_0, \pm\rangle = \pm 0.749 \left| \mp \frac{1}{2} \right\rangle \mp 0.045 \left| \pm \frac{7}{2} \right\rangle \mp 0.661 \left| \mp \frac{9}{2} \right\rangle. \quad (9)$$

Similarly, one can obtain the wavefunctions of the higher energy doublets by putting the appropriate coefficients from Table II in Eq. (8).

In the absence of magnetic correlations, the thermodynamic properties at low temperatures are expected to be influenced significantly by the low-energy CEF excitations. In NKNNO, because of a small energy gap between the ground state and the first excited states, these CEF levels are expected to dominate the low temperature specific heat as observed in NaYbSe₂ [42] and KErTe₂ [41]. To study the effect of CEF excitations on specific heat, we calculated single-ion specific heat [$C_{\text{CEF}}(T)$] at different magnetic fields (see Appendix C) using the energy eigenvalues in Table II and taking into account the Zeeman splitting of the CEF levels [see Fig. 9(b)]. Here, we have taken $g \simeq 2.47$. The calculated results are presented in Fig. 4(d). In zero field, there is only one transition from ground state doublet to the first excited state doublet, and the calculations yield a broad maximum in C_{CEF} at around ~ 9 K. The CEF contribution to the specific heat approaches zero below about 2.4 K in contrast to the low-temperature upturn observed in the experimental C_{mag} . This suggests that the low-temperature upturn in zero-field C_{mag} originates from spin-exchange interactions.

When the magnetic field is applied, the ground state and the first excited state doublets split further and become a four-level system. All the possible transitions between the energy levels are shown in Fig. 9(b). The calculated C_{CEF} results in two broad maxima reproduc-

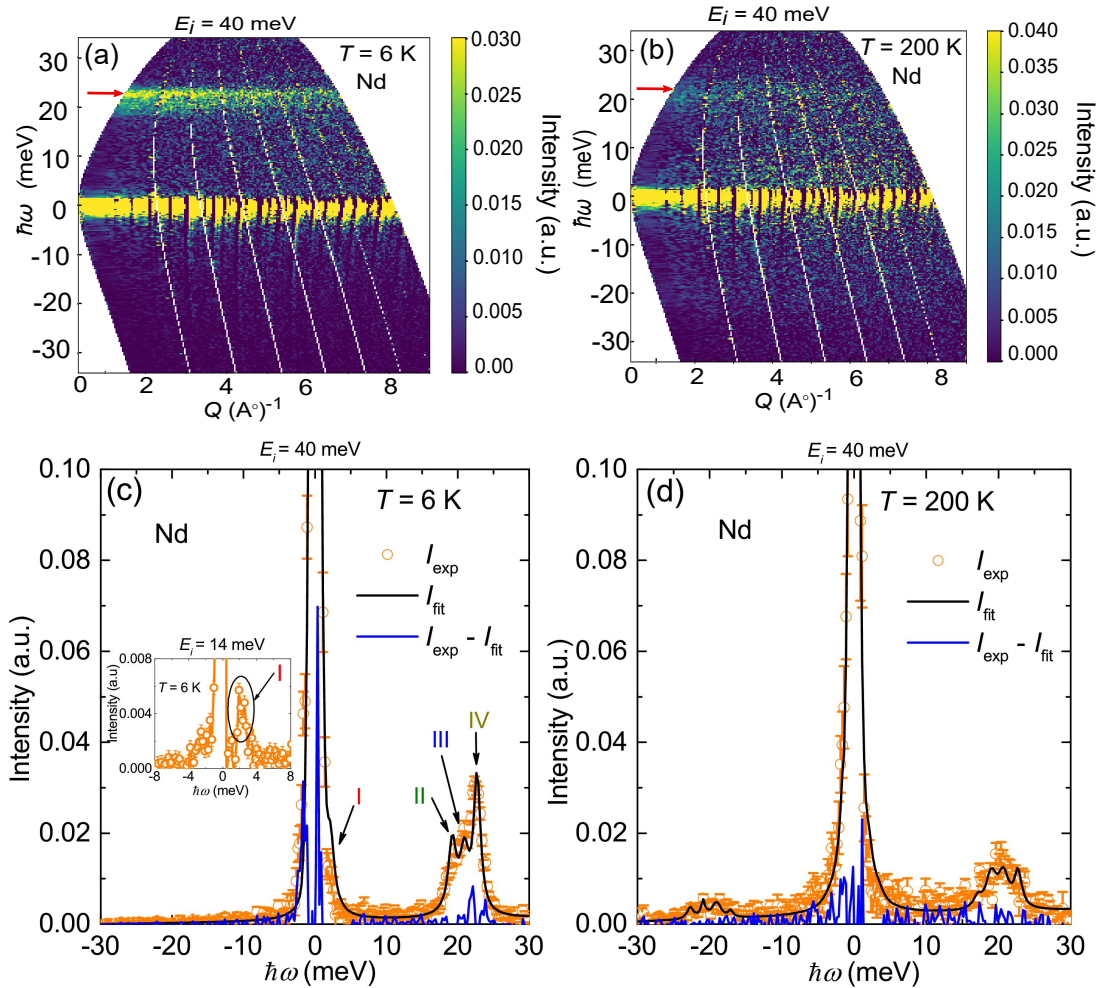


FIG. 7. INS spectra $S(Q, \omega)$ of NKNNO at (a) $T = 6$ K and (b) $T = 200$ K, after subtracting the phonon scattering contribution as discussed in the main text. The red arrow indicates the high-energy CEF excitations. The INS spectral intensity as a function of energy transfer at (c) $T = 6$ K and (d) $T = 200$ K, obtained by integrating intensity in the low wave vector $0 \leq Q \leq 3 \text{ \AA}^{-1}$ regime. The arrows point to the CEF modes (I, II, III, and IV). Black solid line is the corresponding fit using the CEF Hamiltonian. Blue solid line represents the difference between the observed and fitted intensities. Inset of (c): INS intensity vs energy transfer data at $T = 6$ K for $E_i = 14$ meV after subtracting the phonon contribution. The arrow marks the CEF excitations at around 2 meV.

ing our experimental $C_{\text{mag}}(T)$. At $\mu_0 H = 1$ T, the low-temperature maximum at $T^{**} \sim 0.5$ K is due to the transition between the Zeeman levels in the ground state doublet. The high-temperature maximum at $T^* \sim 9$ K can be attributed to the superposition of transitions between the ground state and the first excited state doublets as well as the transitions among the split excited state doublets. With increasing field, the maximum at T^{**} moves towards high temperatures while the one at T^* remains temperature independent but with an increasing line broadening, consistent with the experimental $C_{\text{mag}}(T)$ data. In Fig. 4(d), we have also separately shown the contributions from excitations of the Zeeman split ground state doublet and superposition of excitations among the Zeeman split ground state and first excited state doublets at $\mu_0 H = 2$ T to highlight that they

correspond to the low- T and high- T broad maxima, respectively. Please note that the remaining CEF energy levels (19.2, 20.9, and 22.7 meV) are much higher in energy than the ground state and first excited state. Therefore, the contributions from these higher CEF levels are negligible within our measured temperature range.

For a comparison with the experimental data, we made a 2D contour plot of $C_{\text{CEF}}(T, H)$ and plotted T^* and T^{**} vs H in Fig. 10. The magnetic field variation of T^* and T^{**} obtained from the calculations match with that obtained from the experimental $C_{\text{mag}}(T)$ data. A small difference in the values of T^* and T^{**} from the experiment and theory could be due to the presence of a weak magnetic exchange interaction between the Nd^{3+} ions that is neglected in our calculations.

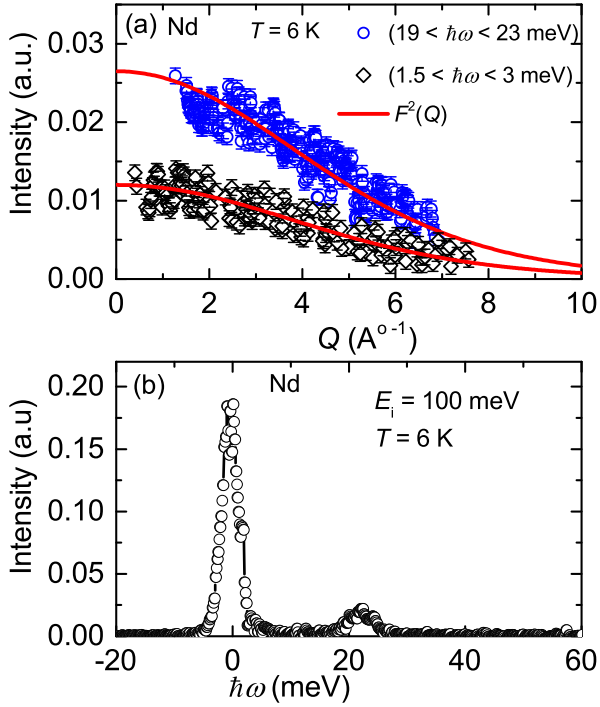


FIG. 8. (a) Q -dependence of INS intensity at $T = 6$ K, obtained by integrating in the transfer energy range 19-23 meV and 1.5-3 meV for the $E_i = 40$ meV data. The red solid lines are the square of magnetic form-factor [$F^2(Q)$] of Nd^{3+} ion. (b) The INS intensity versus energy transfer spectrum of NKNNO with $E_i = 100$ meV at $T = 6$ K, after subtracting the phonon part for the wave-vector range $0 \leq Q \leq 3 \text{ \AA}^{-1}$.

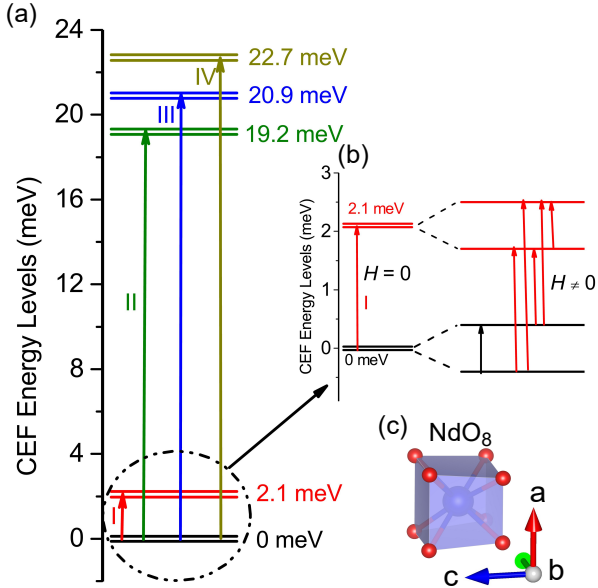


FIG. 9. (a) Schematic representation of CEF excitation energy levels (0, 2.11, 19.22, 20.92, and 22.7 meV) obtained from the zero-field INS data. The arrows indicate the CEF transitions between the states corresponding to the peaks observed in the INS data at $T = 6$ K. (b) Zeeman splitting of the ground and the first excited Kramer's doublets. (c) Distorted NdO_8 cube formed by Nd^{3+} ion that generates CEF.

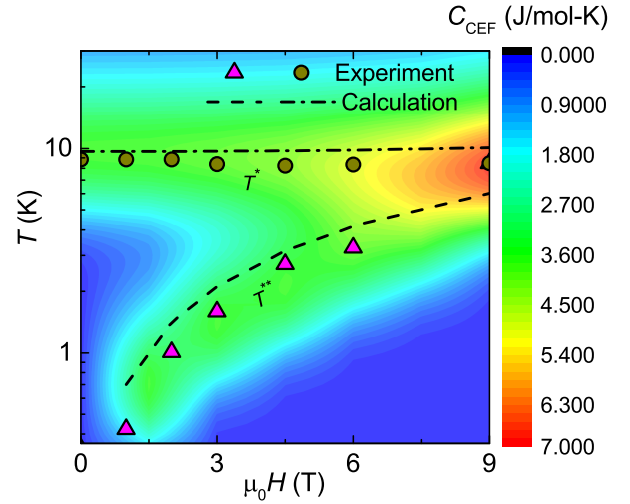


FIG. 10. 2D contour plot of C_{CEF} with field and temperature. On top of this plot, T^* and T^{**} obtained from the experimental C_{mag} (symbols) [from Fig. 4(b)] and calculated C_{CEF} (dashed line) [from Fig. 4(d)] are shown.

IV. DISCUSSION

We studied the ground state properties of an unexplored rare-earth-based FSL system NKNNO through thermodynamic and INS measurements. The low- T value of $\theta_{\text{CW}}^{\text{LT}} \simeq -0.6$ K indicates a weak AFM interaction between the Nd^{3+} ions. The dipolar magnetic interaction of the system is calculated to be $E_{\text{dip}} \simeq \frac{\mu_0 g^2 \mu_B^2 J_{\text{eff}}^2}{4\pi d^3} \simeq 0.015$ K [51]. Here, $d = a/\sqrt{2} \simeq 4.05 \text{ \AA}$ is the distance between NN Nd^{3+} ions, μ_0 is the permeability of free space, $J_{\text{eff}} = 1/2$, and $g \simeq 2.47$. This value of dipolar coupling is about one order of magnitude smaller than $\theta_{\text{CW}}^{\text{LT}}$, suggesting that the magnetic exchange interaction dominates over the dipole-dipole interaction. No magnetic LRO sets in down to 0.4 K possibly due to the magnetic frustration and/or two-dimensional geometry of the spin-lattice. The magnetization and specific heat data indicate that the ground state is pseudo-spin-1/2 ($J_{\text{eff}} = 1/2$). Typically, for compounds with $J_{\text{eff}} = 1/2$ ground state, the dimensionless ratio should have a value $R \equiv \left(\frac{\mu_{\text{eff}}}{\mu_{\text{sat}}}\right)^2 = 3$. This squared moment ratio for NKNNO in the low- T regime is estimated to be $R_{\text{exp}} \simeq 3.06$, which confirms that the lowest Kramer's doublet with $J_{\text{eff}} = 1/2$ is the ground state [52]. From the CEF energy diagram, the energy gap between the ground state and first excited state doublets is found to be about ~ 25 K (~ 2.1 meV). Hence, it is indeed expected that below this temperature scale, the lowest Kramer's doublet with $J_{\text{eff}} = 1/2$ should be manifested as the ground state of the compound.

As discussed above, the wave functions [Eq. (9)] of the ground-state doublet are the linear combinations of $|\pm \frac{1}{2}\rangle$, $|\pm \frac{7}{2}\rangle$, and $|\pm \frac{9}{2}\rangle$ states. The weight factors of $|\pm \frac{1}{2}\rangle$ and $|\pm \frac{9}{2}\rangle$ are found to be larger compared to that of $|\pm \frac{7}{2}\rangle$.

Thus, the obtained large coefficient of $|\pm\frac{1}{2}\rangle$ in the CEF ground state wave function implies that the raising (J_+) and lowering (J_-) operators set a very high probability of quantum tunneling between these two states. At the same time, a significant value of the coefficient of $|\pm\frac{9}{2}\rangle$ also indicates the classical nature of the ground state. Nevertheless, the sizable contribution from $|\pm\frac{1}{2}\rangle$ to the ground state doublet might facilitate strong quantum effects in NKNNO and hence QSL at low temperatures. Our findings are similar to that reported for the other rare-earth-based magnets (Na,K,Cs)Er(S,Se)₂ [16, 53].

V. SUMMARY

We present the first experimental study of an Nd³⁺-based FSL compound NKNNO via magnetization, specific heat, ESR, and INS measurements. It shows the development of magnetic correlations below ~ 1 K in zero-field though no magnetic LRO is detected down to 0.4 K, consistent with the low CW temperature obtained from the $\chi(T)$ analysis. Zero-field specific heat data manifest a single broad maximum at $T^* \simeq 9$ K due to CEF excitations and a low temperature upturn reminiscent of magnetic correlations. An external magnetic field suppresses the weak magnetic correlations and produces two broad maxima in the low-temperature regime, mimicking the excitations among the Zeeman split low energy CEF doublets. INS experiments reveal transitions between the CEF levels, enabling the fitting of CEF parameters to the energies and intensities of these modes. The ground state doublet has a significant $J_z = \pm 1/2$ component in the wave function which indicates the strong quantum effects in this compound at low-temperatures. The small energy gap between the ground state and first excited state of the CEF levels favours Kramers' doublet with $J_{\text{eff}} = 1/2$ ground state at low temperatures, consistent with the findings from magnetization and specific heat data. Finally, using the CEF energy eigenvalues obtained from INS and g -value from ESR experiments we computed $C_{\text{CEF}}(T)$ in different fields which reproduce the positions of the broad maxima in experimental specific heat. This is a clear demonstration of the effect of CEF excitations in the low-temperature specific heat data. To determine whether NKNNO develops magnetic LRO or displays more exotic QSL or spin nematic behaviour at $T = 0$, measurements at temperatures lower than 0.4 K are required.

VI. ACKNOWLEDGMENTS

SG and RN would like to acknowledge SERB, India for financial support bearing sanction Grant No. CRG/2022/000997. SG was supported by the Prime Minister's Research Fellowship (PMRF) scheme and SERB (ITS), Government of India. NBC was supported by the Danish National Committee for Research

Infrastructure (NUFI) through the ESS-Lighthouse Q-MAT and by the Danish Agency for Science, Technology, and Innovation through the instrument centre Danscatt. Experiments at the ISIS Neutron and Muon Source were supported by a beamtime allocation RB2310534 from the Science and Technology Facilities Council. Data is available here: <https://doi.org/10.5286/ISIS.E.RB2310534>.

VII. APPENDIX A:

The intensity recorded in a neutron scattering experiment is simply the partial differential scattering cross-section $\frac{d^2\sigma}{d\omega d\Omega}$ convolved with the instrumental resolution function. For a powder sample, the contribution from CEF level transitions from an initial state $|\psi_i\rangle$ of energy E_i^{CEF} to a final state $|\psi_f\rangle$ of energy E_f^{CEF} can be written as [46].

$$\frac{d^2\sigma}{d\omega d\Omega} = \frac{k_f}{k_i} S(Q, \omega). \quad (10)$$

where \mathbf{k}_i and \mathbf{k}_f are the wave vectors of the incident and scattered neutrons and the dynamic structure factor is given by

$$S(Q, \omega) = CF^2(Q)e^{-2W(Q)} \times \sum_{\alpha=x,y,z} \sum_{i,f} p_i \left| \langle \psi_f | \hat{J}_\alpha | \psi_i \rangle \right|^2 \delta(\hbar\omega + E_i - E_f). \quad (11)$$

Here C is a numerical constant, and the transitions between the CEF levels are caused by angular momentum operators \hat{J}_α ($\alpha = x, y, z$) giving rise to peaks in the spectrum when the neutron energy transfer to the sample $E_i^n - E_f^n = \hbar\omega$ equals the difference between CEF levels $E_f - E_i$. The factor $p_i = e^{-\frac{E_i}{k_B T}} / \sum_i e^{-\frac{E_i}{k_B T}}$ reflects the thermal occupation probability for the initial CEF state. The factor $F(Q)$ is the magnetic formfactor reflecting the spatial extent of the spin-density. In the dipole approximation [46], one can write $F(Q) = \langle j_0(Q) \rangle + \frac{2-g_J}{g_J} \langle j_2(Q) \rangle = \left[\sum_i A_i e^{-a_i Q^2} + D \right] + \frac{2-g_J}{g_J} \left[\sum_i A'_i Q^2 e^{-a'_i Q^2} + D' Q^2 \right]$, where, $A_i, A'_i, a_i, a'_i, D,$ and D' are the magnetic form factor coefficients. These coefficients for Nd³⁺ ion are tabulated in Ref. [54]. Finally, $e^{-2W(Q)}$ is the Debye-Waller factor coming from the thermal motion of the magnetic ion. At low temperatures, the thermal motion of the ion is negligible. Therefore, one can neglect the Q dependence of the Debye-Waller factor at low temperatures [i.e. $e^{-2W(Q)} \simeq 1$].

TABLE II. Energy eigenvalues and the coefficients ($C_{m_J}^{k,\pm}$) corresponding to different eigenstates of the CEF Hamiltonian for NKNNO.

E (meV)	$ - \frac{9}{2}\rangle$	$ - \frac{7}{2}\rangle$	$ - \frac{5}{2}\rangle$	$ - \frac{3}{2}\rangle$	$ - \frac{1}{2}\rangle$	$ \frac{1}{2}\rangle$	$ \frac{3}{2}\rangle$	$ \frac{5}{2}\rangle$	$ \frac{7}{2}\rangle$	$ \frac{9}{2}\rangle$
0.00	-0.661	0	0	0	0.749	0	0	0	-0.045	0
0.00	0	0.045	0	0	0	-0.749	0	0	0	0.661
2.11	0	0	0	-0.764	0	0	0	-0.644	0	0
2.11	0	0	-0.644	0	0	0	-0.764	0	0	0
19.22	0	0.973	0	0	0	-0.117	0	0	0	-0.1982
19.22	-0.1982	0	0	0	-0.117	0	0	0	0.973	0
20.92	0	0	-0.764	0	0	0	0.644	0	0	0
20.92	0	0	0	-0.644	0	0	0	0.764	0	0
22.70	0	-0.225	0	0	0	-0.652	0	0	0	-0.723
22.70	-0.723	0	0	0	-0.652	0	0	0	-0.225	0

VIII. APPENDIX B:

Steven operators in Eq. (7) can be expressed in terms of angular momentum operators J_+ , J_- , and J_z as [55]

$$\begin{aligned}\hat{O}_2^0 &= [3J_z^2 - X], \\ \hat{O}_4^0 &= [35J_z^4 - (30X - 25)J_z^2 + 3X^2 - 6X], \\ \hat{O}_4^4 &= \frac{1}{2}[J_+^4 + J_-^4],\end{aligned}\quad (12)$$

$$\begin{aligned}\hat{O}_6^0 &= [231J_z^6 - (315X - 735)J_z^4 + \\ & (105X^2 - 525X + 294)J_z^2 - 5X^3 + 40X^2 - 60X],\end{aligned}\quad (13)$$

$$\hat{O}_6^4 = \frac{1}{4}[(J_+^4 + J_-^4)(11J_z^2 - X - 38) + \quad (15)$$

$$(11J_z^2 - X - 38)(J_+^4 + J_-^4)]. \quad (16)$$

$$(17)$$

Here, $X = J(J + 1)$.

According to the point charge model, the CEF param-

eters (B_l^m) in Eq. (7) can be written as [34, 56]

$$B_l^m = \frac{4\pi}{2l+1} \times \frac{|e|^2}{4\pi\epsilon_0} \sum_i \frac{q_i}{r_i^{l+1}} a_0^l \langle r^l \rangle Z_l^m(\theta_i, \phi_i). \quad (18)$$

where q_i is the charge of the i^{th} point charge, r_i , θ_i , and ϕ_i are the relative polar coordinates of the i^{th} point charge from the magnetic ion. a_0 is the Bohr radius and $\langle r^l \rangle$ is the l^{th} order expectation value of the radial wave function of the magnetic ion.

IX. APPENDIX C:

Specific heat (C_{CEF}) for a N level system can be written as

$$C_{\text{CEF}}(N) = R\beta^2 \frac{1}{Z^2} \sum_{j>i}^N (E_j - E_i)^2 e^{-(E_i+E_j)\beta}, \quad (19)$$

where, R is the universal gas constant, $\beta = \frac{1}{k_B T}$, and Z ($= \sum_i e^{-\frac{E_i}{k_B T}}$) is the partition function. For NKNNO, in zero-field, the ground state doublet is separated from the first excited state doublet by an energy gap Δ (~ 2.11 meV). In the presence of a magnetic field, these doublets are split into four energy levels. Therefore, in the calculations shown in Fig. 4(d), we have taken $N = 4$.

-
- [1] L. Savary and L. Balents, Quantum spin liquids: a review, *Rep. Prog. Phys.* **80**, 016502 (2016).
- [2] L. Wang and A. W. Sandvik, Critical Level Crossings and Gapless Spin Liquid in the Square-Lattice Spin-1/2 $J_1 - J_2$ Heisenberg Antiferromagnet, *Phys. Rev. Lett.* **121**, 107202 (2018).
- [3] N. Shannon, T. Momoi, and P. Sindzingre, Nematic Order in Square Lattice Frustrated Ferromagnets, *Phys. Rev. Lett.* **96**, 027213 (2006).
- [4] R. Nath, Y. Furukawa, F. Borsa, E. E. Kaul, M. Baenitz, C. Geibel, and D. C. Johnston, Single-crystal ^{31}P NMR studies of the frustrated square-lattice compound $\text{Pb}_2\text{VO}(\text{PO}_4)_2$, *Phys. Rev. B* **80**, 214430 (2009).
- [5] R. Nath, A. A. Tsirlin, H. Rosner, and C. Geibel, Magnetic properties of $\text{BaCdVO}(\text{PO}_4)_2$: A strongly frustrated spin- $\frac{1}{2}$ square lattice close to the quantum critical regime, *Phys. Rev. B* **78**, 064422 (2008).
- [6] S. Guchhait, D. V. Ambika, Q.-P. Ding, M. Uhlarz, Y. Furukawa, A. A. Tsirlin, and R. Nath,

- Deformed spin- $\frac{1}{2}$ square lattice in antiferromagnetic NaZnVOPO₄(HPO₄), *Phys. Rev. B* **106**, 024426 (2022).
- [7] P. Babkevich, V. M. Katukuri, B. Fåk, S. Rols, T. Fennell, D. Pajić, H. Tanaka, T. Pardini, R. R. P. Singh, A. Mitrushchenkov, O. V. Yazyev, and H. M. Rønnow, Magnetic Excitations and Electronic Interactions in Sr₂CuTeO₆: A Spin-1/2 Square Lattice Heisenberg Antiferromagnet, *Phys. Rev. Lett.* **117**, 237203 (2016).
- [8] M. Watanabe, N. Kurita, H. Tanaka, W. Ueno, K. Matsui, T. Goto, and M. Hagihala, Contrasting magnetic structures in SrLaCuSbO₆ and SrLaCuNbO₆: Spin- $\frac{1}{2}$ quasi-square-lattice $J_1 - J_2$ Heisenberg antiferromagnets, *Phys. Rev. B* **105**, 054414 (2022).
- [9] A. A. Tsirlin, B. Schmidt, Y. Skourski, R. Nath, C. Geibel, and H. Rosner, Exploring the spin- $\frac{1}{2}$ frustrated square lattice model with high-field magnetization studies, *Phys. Rev. B* **80**, 132407 (2009).
- [10] O. Mustonen, S. Vasala, K. P. Sadrollahi, E. Schmidt, C. Baines, H. C. Walker, I. Terasaki, F. J. Litterst, E. Baggio-Saitovitch, and M. Karppinen, Spin-liquid-like state in a spin-1/2 square-lattice antiferromagnet perovskite induced by d¹⁰-d⁰ cation mixing, *Nat. Commun.* **9**, 1085 (2018).
- [11] A. A. Tsirlin and H. Rosner, Extension of the spin- $\frac{1}{2}$ frustrated square lattice model: The case of layered vanadium phosphates, *Phys. Rev. B* **79**, 214417 (2009).
- [12] Y. Li, D. Adroja, P. K. Biswas, P. J. Baker, Q. Zhang, J. Liu, A. A. Tsirlin, P. Gegenwart, and Q. Zhang, Muon Spin Relaxation Evidence for the U(1) Quantum Spin-Liquid Ground State in the Triangular Antiferromagnet YbMgGaO₄, *Phys. Rev. Lett.* **117**, 097201 (2016).
- [13] J. G. Rau and M. J. P. Gingras, Magnitude of quantum effects in classical spin ices, *Phys. Rev. B* **92**, 144417 (2015).
- [14] B. Tomasello, C. Castelnovo, R. Moessner, and J. Quintanilla, Single-ion anisotropy and magnetic field response in the spin-ice materials Ho₂Ti₂O₇ and Dy₂Ti₂O₇, *Phys. Rev. B* **92**, 155120 (2015).
- [15] S. Petit, J. Robert, S. Guitteny, P. Bonville, C. Decorse, J. Ollivier, H. Mutka, M. J. P. Gingras, and I. Mirebeau, Order by disorder or energetic selection of the ground state in the XY pyrochlore antiferromagnet Er₂Ti₂O₇: An inelastic neutron scattering study, *Phys. Rev. B* **90**, 060410 (2014).
- [16] S. Gao, F. Xiao, K. Kamazawa, K. Ikeuchi, D. Biner, K. W. Krämer, C. Rüegg, and T.-h. Arima, Crystal electric field excitations in the quantum spin liquid candidate NaErS₂, *Phys. Rev. B* **102**, 024424 (2020).
- [17] R. Sibille, N. Gauthier, H. Yan, M. Ciomaga Hatnean, J. Ollivier, B. Winn, U. Filges, G. Balakrishnan, M. Kenzelmann, N. Shannon, and T. Fennell, Experimental signatures of emergent quantum electrodynamics in Pr₂Hf₂O₇, *Nat. Phys.* **14**, 711 (2018).
- [18] U. Arjun, K. Brinda, M. Padmanabhan, and R. Nath, Magnetic properties of layered rare-earth oxy-carbonates Ln₂O₂CO₃ (Ln=Nd, Sm, and Dy), *Solid State Commun.* **240**, 1 (2016).
- [19] S. Nandi, Y. Jana, D. Swarnakar, J. Alam, P. Bag, and R. Nath, Magnetization process and specific heat properties of geometrically frustrated pyrochlores R₂FeSbO₇ (R³⁺ = Dy, Y) and spin-ice magnetic phase in Dy₂FeSbO₇, *J. Alloys Compd.* **714**, 318 (2017).
- [20] Z. Ma, S. Zheng, Y. Chen, R. Xu, Z.-Y. Dong, J. Wang, H. Du, J. P. Embs, S. Li, Y. Li, Y. Zhang, M. Liu, R. Zhong, J.-M. Liu, and J. Wen, Possible gapless quantum spin liquid behavior in the triangular-lattice Ising antiferromagnet PrMgAl₁₁O₁₉, *Phys. Rev. B* **109**, 165143 (2024).
- [21] K. Somesh, S. S. Islam, S. Mohanty, G. Simutis, Z. Guguchia, C. Wang, J. Sichelschmidt, M. Baenitz, and R. Nath, Absence of magnetic order and emergence of unconventional fluctuations in the $J_{\text{eff}} = \frac{1}{2}$ triangular-lattice antiferromagnet YbBO₃, *Phys. Rev. B* **107**, 064421 (2023).
- [22] A. Zorko, F. Bert, P. Mendels, K. Marty, and P. Bordet, Ground State of the Easy-Axis Rare-Earth Kagome Langanite Pr₃Ga₅SiO₁₄, *Phys. Rev. Lett.* **104**, 057202 (2010).
- [23] V. Simonet, R. Ballou, J. Robert, B. Canals, F. Hippert, P. Bordet, P. Lejay, P. Fouquet, J. Ollivier, and D. Braithwaite, Hidden Magnetic Frustration by Quantum Relaxation in Anisotropic Nd Langanite, *Phys. Rev. Lett.* **100**, 237204 (2008).
- [24] K. M. Ranjith, D. Dmytriieva, S. Khim, J. Sichelschmidt, S. Luther, D. Ehlers, H. Yasuoka, J. Wosnitzer, A. A. Tsirlin, H. Kühne, and M. Baenitz, Field-induced instability of the quantum spin liquid ground state in the $J_{\text{eff}} = \frac{1}{2}$ triangular-lattice compound NaYbO₂, *Phys. Rev. B* **99**, 180401 (2019).
- [25] T. Fennell, M. Kenzelmann, B. Roessli, M. K. Haas, and R. J. Cava, Power-Law Spin Correlations in the Pyrochlore Antiferromagnet Tb₂Ti₂O₇, *Phys. Rev. Lett.* **109**, 017201 (2012).
- [26] J. Gaudet, A. M. Hallas, A. I. Kolesnikov, and B. D. Gaulin, Effect of chemical pressure on the crystal field states of erbium pyrochlore magnets, *Phys. Rev. B* **97**, 024415 (2018).
- [27] Z. L. Dun, X. Li, R. S. Freitas, E. Arrighi, C. R. Dela Cruz, M. Lee, E. S. Choi, H. B. Cao, H. J. Silverstein, C. R. Wiebe, J. G. Cheng, and H. D. Zhou, Antiferromagnetic order in the pyrochlores R₂Ge₂O₇ (R = Er, Yb), *Phys. Rev. B* **92**, 140407 (2015).
- [28] K. Kimura, S. Nakatsuji, J.-J. Wen, C. Broholm, M. B. Stone, E. Nishibori, and H. Sawa, Quantum fluctuations in spin-ice-like Pr₂Zr₂O₇, *Nat. Commun.* **4**, 1934 (2013).
- [29] E. Lhotel, S. Petit, S. Guitteny, O. Florea, M. Ciomaga Hatnean, C. Colin, E. Ressouche, M. R. Lees, and G. Balakrishnan, Fluctuations and All-In-All-Out Ordering in Dipole-Octupole Nd₂Zr₂O₇, *Phys. Rev. Lett.* **115**, 197202 (2015).
- [30] U. Arjun, K. M. Ranjith, A. Jesche, F. Hirschberger, D. D. Sarma, and P. Gegenwart, Adiabatic demagnetization refrigeration to millikelvin temperatures with the distorted square lattice magnet NaYbGeO₄, *Phys. Rev. B* **108**, 224415 (2023).
- [31] V. K. Singh, K. Nam, M. Barik, K. Boya, E. Kermarrec, P. Khuntia, K. H. Kim, S. Bhowal, and B. Koteswararao, Bi₂YbO₄Cl: A two-dimensional square-lattice compound with $J_{\text{eff}} = \frac{1}{2}$ magnetic moments, *Phys. Rev. B* **109**, 075128 (2024).
- [32] I. P. Roof, T.-C. Jagau, W. G. Zeier, M. D. Smith, and H.-C. zur Loye, Crystal growth of a new series of complex niobates, LnKNaNbO₅ (Ln = La, Pr, Nd, Sm, Eu, Gd, and Tb): structural properties and photoluminescence, *Chem. Mater.* **21**, 1955 (2009).
- [33] J. Rodríguez-Carvajal, Recent advances in magnetic structure determination by neutron powder diffraction, *Physica B Condens. Matter* **192**, 55 (1993).

- [34] O. Arnold, J. Bilheux, J. Borreguero, A. Buts, S. Campbell, L. Chapon, M. Doucet, N. Draper, R. Ferraz Leal, M. Gigg, V. Lynch, A. Markvardsen, D. Mikkelsen, R. Mikkelsen, R. Miller, K. Palmen, P. Parker, G. Passos, T. Perring, P. Peterson, S. Ren, M. Reuter, A. Savici, J. Taylor, R. Taylor, R. Tolchenov, W. Zhou, and J. Zikovsky, Mantid—Data analysis and visualization package for neutron scattering and μ SR experiments, *Nucl. Instrum. Methods Phys. Res. A* **764**, 156 (2014).
- [35] S. Mugiraneza and A. M. Hallas, Tutorial: a beginner’s guide to interpreting magnetic susceptibility data with the Curie-Weiss law, *Commun. Phys.* **5**, 95 (2022).
- [36] M. Pula, S. Sharma, J. Gautreau, S. K. P., A. Kanigel, M. D. Frontzek, T. N. Dolling, L. Clark, S. Dunsiger, A. Ghara, and G. M. Luke, Candidate for a quantum spin liquid ground state in the Shastry-Sutherland lattice material $\text{Yb}_2\text{Be}_2\text{GeO}_7$, *Phys. Rev. B* **110**, 014412 (2024).
- [37] P. Biswal, S. Guchhait, S. Ghosh, S. N. Sarangi, D. Samal, D. Swain, M. Kumar, and R. Nath, Crystal structure and magnetic properties of the spin- $\frac{1}{2}$ frustrated two-leg ladder compounds $(\text{C}_4\text{H}_{14}\text{N}_2)\text{Cu}_2\text{X}_6$ ($X = \text{Cl}$ and Br), *Phys. Rev. B* **108**, 134420 (2023).
- [38] C. Kittel, *Introduction to Solid State Physics* (Wiley, 2004).
- [39] M. Bouvier, P. Lethuillier, and D. Schmitt, Specific heat in some gadolinium compounds. I. Experimental, *Phys. Rev. B* **43**, 13137 (1991).
- [40] J. Xing, L. D. Sanjeewa, J. Kim, W. R. Meier, A. F. May, Q. Zheng, R. Custelcean, G. R. Stewart, and A. S. Sefat, Synthesis, magnetization, and heat capacity of triangular lattice materials NaErSe_2 and KErSe_2 , *Phys. Rev. Mater.* **3**, 114413 (2019).
- [41] W. Liu, Z. Zhang, D. Yan, J. Li, Z. Zhang, J. Ji, F. Jin, Y. Shi, and Q. Zhang, Effects of the Crystalline Electric Field in the KErTe_2 Quantum Spin Liquid Candidate, [arXiv:2108.09693](https://arxiv.org/abs/2108.09693) (2021).
- [42] K. M. Ranjith, S. Luther, T. Reimann, B. Schmidt, P. Schlender, J. Sichelschmidt, H. Yasuoka, A. M. Strydom, Y. Skourski, J. Wosnitza, H. Kühne, T. Doert, and M. Baenitz, Anisotropic field-induced ordering in the triangular-lattice quantum spin liquid NaYbSe_2 , *Phys. Rev. B* **100**, 224417 (2019).
- [43] S. Mohanty, S. S. Islam, N. Winterhalter-Stocker, A. Jesche, G. Simutis, C. Wang, Z. Guguchia, J. Sichelschmidt, M. Baenitz, A. A. Tsirlin, P. Gegenwart, and R. Nath, Disordered ground state in the spin-orbit coupled $J_{\text{eff}} = \frac{1}{2}$ distorted honeycomb magnet BiYbGeO_5 , *Phys. Rev. B* **108**, 134408 (2023).
- [44] J. Sichelschmidt, P. Schlender, B. Schmidt, M. Baenitz, and T. Doert, Electron spin resonance on the spin-1/2 triangular magnet NaYbS_2 , *J. Phys.: Condens. Matter* **31**, 205601 (2019).
- [45] R. Orbach, Spin-lattice relaxation in rare-earth salts, *Proc. R. Phys. Soc. A* **264**, 458 (1961).
- [46] A. Boothroyd, *Principles of Neutron Scattering from Condensed Matter* (OUP Oxford, 2020).
- [47] K. W. H. Stevens, Matrix elements and operator equivalents connected with the magnetic properties of rare earth ions, *Proc. Phys. Soc. Section A* **65**, 209 (1952).
- [48] M. Hutchings, *Point-Charge Calculations of Energy Levels of Magnets*, Solid State Physics, Vol. 16 (Academic Press, 1964) p. 227.
- [49] A. Furrer, J. Mesot, and T. Straessle, *Neutron Scattering In Condensed Matter Physics*, Series On Neutron Techniques And Applications (World Scientific Publishing Company, 2009).
- [50] R. Yamamoto, M. D. Le, D. T. Adroja, Y. Shimura, T. Takabatake, and T. Onimaru, Inelastic neutron scattering study of crystalline electric field excitations in the caged compounds $\text{NdT}_2\text{Zn}_{20}$ ($T = \text{Co, Rh, and Ir}$), *Phys. Rev. B* **107**, 075114 (2023).
- [51] J. Xiang, C. Su, N. Xi, Z. Fu, Z. Chen, H. Jin, Z. Chen, Z.-J. Mo, Y. Qi, J. Shen, L. Zhang, W. Jin, W. Li, P. Sun, and G. Su, Dipolar Spin Liquid Ending with Quantum Critical Point in a Gd-based compound, [arXiv:2301.03571](https://arxiv.org/abs/2301.03571).
- [52] S. Guo, A. Ghasemi, C. L. Broholm, and R. J. Cava, Magnetism on ideal triangular lattices in $\text{NaBaYb}(\text{BO}_3)_2$, *Phys. Rev. Mater.* **3**, 094404 (2019).
- [53] A. Scheie, V. O. Garlea, L. D. Sanjeewa, J. Xing, and A. S. Sefat, Crystal-field Hamiltonian and anisotropy in KErSe_2 and CsErSe_2 , *Phys. Rev. B* **101**, 144432 (2020).
- [54] E. Prince, *International Tables for Crystallography* (Springer Netherlands, 2004).
- [55] D. J. Newman and B. Ng, *Crystal Field Handbook* (Cambridge University Press, 2000).
- [56] Y. Li, G. Chen, W. Tong, L. Pi, J. Liu, Z. Yang, X. Wang, and Q. Zhang, Rare-Earth Triangular Lattice Spin Liquid: A Single-Crystal Study of YbMgGaO_4 , *Phys. Rev. Lett.* **115**, 167203 (2015).